


# Regulation of Luminescence Properties of the Ultrathin Two-Dimensional Halide Perovskite $\text{Cs}_2\text{PbI}_x\text{Cl}_{4-x}$ ( $x = 0,1,2,3,4$ ) with Ruddlesden-Popper Structure

Jun Luo,<sup>1</sup> Biao Liu,<sup>2</sup> Jun-Liang Yang,<sup>2</sup> and Meng-Qiu Cai<sup>1,\*</sup>

<sup>1</sup>Hunan Provincial Key Laboratory of High-Energy Scale Physics and Applications, School of Physics and Electronics, Hunan University, Changsha 410082, People's Republic of China

<sup>2</sup>Hunan Key Laboratory for Super-microstructure and Ultrafast Process, School of Physics and Electronics, Central South University, Changsha 410083, Hunan, China

 (Received 21 March 2023; revised 18 July 2023; accepted 26 July 2023; published 18 August 2023)

The synthesized two-dimensional (2D) Ruddlesden-Popper (RP) all-inorganic mixed halogen perovskite,  $\text{Cs}_2\text{PbI}_x\text{Cl}_{4-x}$  ( $x = 2$ ) has attracted extensive attention due to its excellent luminescence properties and environmental stability. However, the regulation of halogen ratio and halogen replacement sites on the luminescence properties of 2D RP inorganic mixed halogen perovskite remains unknown. In this paper, the luminescence properties containing band structures, effective mass, exciton-binding energies, photoluminescence emission energy, and the transition dipole moment of 2D RP perovskite  $\text{Cs}_2\text{PbI}_x\text{Cl}_{4-x}$  ( $x = 0,1,2,3,4$ ) were studied via density-functional theory. To systematically represent different replacement sites, according to the halogens on the equatorial plane of the octahedron, we divide it into three types. [(1) the halogens on the equatorial plane are I atoms; (2) the halogens on the equatorial plane are Cl atoms; (3) the halogens on the equatorial plane are composed of I and Cl atoms]. The calculation results show that for structures with replacement sites of the same kind, the band gap, photoluminescence emission energy, and transition dipole moment decrease with the increase of the proportion of I atoms, while the opposite is true for exciton-binding energy and effective mass. In addition, among the three types of replacement sites, the quadratic eigenvalue problem-Mix (equatorial plane is composed of I and Cl) type replacement site is the most conducive to the luminescence performance of the material. Our theoretical study will provide guidance for the design and fabrication of highly luminescent 2D RP perovskite.

DOI: [10.1103/PhysRevApplied.20.024047](https://doi.org/10.1103/PhysRevApplied.20.024047)

## I. INTRODUCTION

Two-dimensional (2D) Ruddlesden-Popper (RP) halide perovskites have great potential in the field of luminescence due to their large exciton-binding energy, high photoluminescence yield, and tunability [1]. Some researchers studied the photoelectric properties of 2D RP layered perovskite and found that the photovoltaic properties weakened and the luminescence properties became stronger with the decrease of the number of layers. For example, Zhao *et al.* studied 2D RP organo-inorganic hybrid perovskite  $(\text{PEA})_2\text{PbI}_4$ , and found that it has a high electron-hole recombination rate, so it is not suitable for photovoltaic materials, and with the increase of layer number, the carrier migration rate increases, and the exciton-binding energy decreases [2]. Pan *et al.* also found that the monolayer of 2D RP perovskite  $\text{Cs}_2\text{PbI}_2\text{Cl}_2$  with maximum exciton-binding energy and minimum carrier

migration rate may be suitable for luminescent materials when studying the effect of layer number on photoelectric properties of 2D RP perovskite [3]. Therefore, the monolayer structure should be considered first to explore suitable luminescent materials in 2D-layered RP perovskite. Moreover, previous studies have shown that halogen substitution can improve the photoelectric properties of halogen perovskite materials. For example, Zeng *et al.* calculated the photoelectric properties of 2D RP double perovskite  $\text{Cs}_4\text{AgBiX}_8$  ( $X = \text{Cl}, \text{Br}, \text{I}$ ) and found that the band gap, light-absorption intensity, exciton-binding energy, and carrier mobility change monotonically with halogen substitution [4]. Chen *et al.* studied the effect of halogen substitution on the electronic and optical properties of 2D lead-free hybrid perovskites  $(\text{BA})_2\text{GeX}_4$  and  $(\text{BA})_2\text{SnX}_4$  ( $X = \text{I}, \text{Br}, \text{Cl}$ ), and found that as  $X$  changes from Cl to Br to I, the effective mass and band gap decrease monotonically and the optical absorption capacity increase monotonically [5]. However, Carina *et al.* found that when  $x = 1.5$ , 2D halide perovskites  $(\text{Br-PEA})_2\text{PbBr}_x\text{Cl}_{4-x}$  (Br-PEA = 4-bromo phenethylammonium) had the largest PLQY(25.3%) [6], which did

\*mqcai@hnu.edu.cn

not show a monotonic change. Zhang *et al.* found that MAPbBr<sub>3-x</sub>Cl<sub>x</sub> had a stronger photoluminescence performance than MAPbBr<sub>3</sub> and MAPbCl<sub>3</sub>. (MA abbreviates for CH<sub>3</sub>NH<sub>3</sub>), indicating that the mixed halogen may have a better photoluminescence performance [7]. Moreover, Deng *et al.* found that compared with the other two doping sites in RbGe<sub>0.50</sub>Sn<sub>0.50</sub>I<sub>3</sub> perovskite, the equatorial Sn configuration had better electron mobility and optical absorption properties [8]. This indicates that different doping positions of metal atoms can improve the photoelectric properties of perovskite materials. Therefore, we expect to improve the luminescence properties of monolayer 2D RP perovskite and explore the regulation rules by adjusting the halogen composition and halogen replacement position.

In this paper, the band structure, exciton absorption, photoluminescence emission energy, and the transition dipole moment of monolayer 2D RP perovskite Cs<sub>2</sub>PbI<sub>x</sub>Cl<sub>4-x</sub> ( $x = 0, 1, 2, 3, 4$ ) are calculated. By analyzing the outcomes obtained, the effects of halogen composition and halogen replacement position on the luminescence properties of 2D RP all-inorganic perovskite were discussed.

## II. COMPUTATIONAL METHODS

### A. DFT calculations

The Vienna *ab initio* simulation software package (VASP) was used for DFT calculations. The interaction between valence electrons and ion nuclei is considered by the projector augmented-wave (PAW) method. The Perdew, Burke, and Ernzerhof (PBE) models are used to describe the exchange-correlation effects. A cutoff energy of 400 eV is set. The two-dimensional Brillouin zone is sampled using a 4×4×1 Monkhorst-Pack  $k$  mesh. For structural relaxation, the force tolerance standard for each atom is less than 0.02 eV/Å. The band structure is calculated precisely by using the Heyd-Scuseria-Ernzerhof (HSE) hybrid function and considering the spin-orbit-coupling (SOC) effect. The HSE mixing parameter is set to  $\alpha = 43\%$  based on Ref. [9]. All images were created using ORIGIN and VESTA.

### B. Effective mass

The in-plane effective mass ( $m^*$ ) is obtained by the equation

$$m^* = \hbar^2 \left[ \frac{\partial^2 \varepsilon(k)}{\partial k^2} \right]^{-1}. \quad (1)$$

In which the  $k$  is the wave vector along the transport direction and the  $\varepsilon(k)$  represents the energy-band eigenvalues [10].

### C. Exciton-binding energy calculation

The exciton-binding energy is obtained by the following formula [11]:

$$E_B = (2/(\alpha - 1))^2 E_{B,3D} \quad (2)$$

the  $E_{B,3D}$  is the bulk exciton-binding energy, which can be obtained by the formula  $E_{B,3D} = (1/\varepsilon_1)^2 (M_{\text{ex}}/M_0)R_H$ . The  $\varepsilon_1$  is the static dielectric constant contributed by electrons, which can be calculated by using density-functional perturbation theory [12–14],  $M_{\text{ex}}$  means reduced exciton mass, which is expressed  $1/(1/me + 1/mh)$ ,  $M_0$  the free electron mass and  $R_H$  the hydrogen Rydberg constant.  $\alpha$  is the dimension of the structure (bulk,  $\alpha = 3$ , 2D,  $\alpha = 2$ ). In addition, we take monolayer MoS<sub>2</sub> as an example to calculate its exciton binding energy by using the *GW* Bethe-Salpeter equation (BSE) method and Eq. (2) (see Table S4 within the Supplemental Material [41]). By comparing the results calculated by the two methods, it can be found that the exciton-binding energy obtained by the two methods is very close to the experimental value [15–17], which proves the reliability of Eq. (2). Moreover, Eq. (2) has also been used to report exciton-binding energy in many literatures [18–23]. Therefore, in order to save computational resources, only the formula method is used to calculate the exciton-binding energy. The calculation parameters of the *GW* BSE method are included in Fig. S12 within the Supplemental Material [41].

### D. The self-trapping energy ( $E_{\text{ST}}$ )

The self-trapping energy is defined as the excited-state energy difference between the self-trapped exciton (STE) and free exciton (FE) configurations, which is the key parameter to determine whether the material will have self-trapping emission [24,25]. The expression is  $E_{\text{ST}} = E_{\text{STE}} - E_{\text{FE}}$ . The excited-state structure is obtained on the basis of the self-consistent field ( $\Delta$ SCF) method [26]. To do that, we first move an electron from the valence-band maximum (VBM) state to the conduction-band minimum (CBM) state in the 3×3×1 Cs<sub>2</sub>PbI<sub>x</sub>Cl<sub>4-x</sub> supercell. And then keeping their band-state occupation unchanged, relaxing the structure of these compounds and obtaining the optimized excited-state structure. To avoid nonphysical occupancy of the band-edge state, the  $k$  mesh for these calculations is set to 1 × 1 × 1.

### E. The *ab initio* molecular dynamic (AIMD) simulations

AIMD simulations are performed to explore the thermal stability of the 2D RP halogen perovskites at 298.15 K [27]. The Nosé algorithm is employed to manipulate the temperature and the total dynamic steps are set up to 10 000 steps with a time step of 1.0 fs [28].

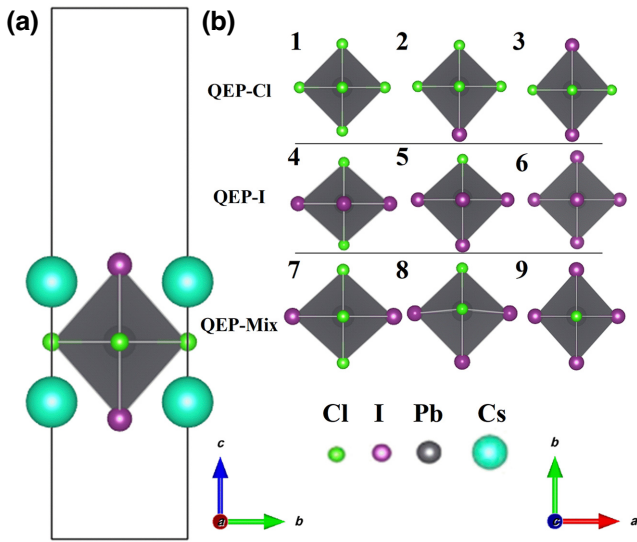


FIG. 1. (a) Crystal structure of the monolayer of 2D RP perovskite  $\text{Cs}_2\text{PbI}_2\text{Cl}_2$ ; (b) octahedral structures with different equatorial plane; 1, 2, and 3 show  ${}^{\text{Cl}}\text{Cs}_2\text{PbCl}_4$ ,  ${}^{\text{Cl}}\text{Cs}_2\text{PbI}_3\text{Cl}_3$ , and  ${}^{\text{Cl}}\text{Cs}_2\text{PbI}_2\text{Cl}_2$  with QEP-Cl structure, respectively. 4, 5, and 6 show  ${}^{\text{I}}\text{Cs}_2\text{PbI}_2\text{Cl}_1$ ,  ${}^{\text{I}}\text{Cs}_2\text{PbI}_3\text{Cl}_1$ , and  ${}^{\text{I}}\text{Cs}_2\text{PbI}_4$  with QEP-I structure, respectively. 7, 8, and 9 show  ${}^{\text{Mix}}\text{Cs}_2\text{PbI}_1\text{Cl}_3$ ,  ${}^{\text{Mix}}\text{Cs}_2\text{PbI}_2\text{Cl}_2$ , and  ${}^{\text{Mix}}\text{Cs}_2\text{PbI}_3\text{Cl}_1$  with QEP-Mix structure, respectively.

### III. RESULTS AND DISCUSSION

Based on the tetragonal crystal structure of 2D RP perovskite  $\text{Cs}_2\text{PbI}_2\text{Cl}_2$  obtained in the experiment [29], the monolayer structure was retained and a 15-angstrom vacuum layer was added along the  $c$  axis to prevent inter-layer interaction. Based on this monolayer structure, we performed halogen replacement and fully optimized the structure to obtain nine structures of the monolayer 2D RP perovskite  $\text{Cs}_2\text{PbI}_x\text{Cl}_{4-x}$  ( $x = 0, 1, 2, 3, 4$ ). The crystal structures and the octahedral structures are shown in Fig. 1. The equatorial plane composition of the octahedron is different due to the different sites of halogen substitution. According to the composition of the equatorial plane of the octahedron, these nine materials are divided into three categories. The first category is that the halogens in the equatorial plane are all Cl atoms [quadratic eigenvalue problem (QEP)-Cl], as shown in Fig. 1(b)(1–3). The second category is that the halogens in the equatorial plane are all I atoms (QEP-I), as shown in Fig. 1(b)(4–6). The third category is that the halogens in the equatorial plane are composed of I atoms and Cl atoms (QEP-Mix), as shown in Fig. 1(b)(7–9). The QEP-Cl structure is labeled as  ${}^{\text{Cl}}\text{Cs}_2\text{PbI}_x\text{Cl}_{4-x}$  ( $x = 0, 1, 2, 3, 4$ ), the QEP-I structure is labeled as  ${}^{\text{I}}\text{Cs}_2\text{PbI}_x\text{Cl}_{4-x}$  ( $x = 0, 1, 2, 3, 4$ ), and the QEP-Mix structure is labeled as  ${}^{\text{Mix}}\text{Cs}_2\text{PbI}_x\text{Cl}_{4-x}$  ( $x = 0, 1, 2, 3, 4$ ).

After obtaining the optimized crystal structure, the HSE + SOC method was used to calculate the projected

band structures of these nine materials, as shown in Fig. 2. The size of the circle corresponds to the relative weight, and each element uses a different color. By comparing the experimental band gap (3.04 eV) with the calculated band gap (2.97 eV) of  ${}^{\text{Cl}}\text{Cs}_2\text{PbI}_2\text{Cl}_2$ , it can be found that the calculated band gap is slightly smaller [29]. This is because the band gap obtained by the experiment is that of the bulk structure. Therefore, the band gap of the bulk structure (Bulk- $\text{Cs}_2\text{PbI}_2\text{Cl}_2$ ) is also calculated to verify the reliability of the method, as shown in Fig. S4 within the Supplemental Material [41]. The calculated value (3.06 eV) is in good agreement with the experimental value. Next, the band results were analyzed. First of all, it can be seen from the figure that all nine materials are direct band gaps, which is favorable for photoluminescence. See the Supplemental Material for a detailed explanation [41]. Secondly, by observing the contribution of each element to the band edge, it can be found that the conduction-band edge of these nine materials is basically contributed by Pb atoms, and the valence-band edge is basically contributed by halogen atoms and Pb atoms together, while Cs atoms hardly contribute. In addition, the contribution of halogen atoms to the valence-band top in the same type of material is positively correlated with the content of halogen atoms. In order to further discuss the effect of halogens on band edges, the partial density of states (PDOS) of these nine materials was calculated, and the calculation results are shown in Fig. S7 within the Supplemental Material [41]. The results show that the valence-band edge is indeed mainly contributed by the  $p$  orbitals of halogen atoms and the  $s$  orbitals of Pb atoms and the conduction band edge is mainly contributed by the  $p$  orbitals of Pb atoms. Previous studies have shown that the atomic orbital composition of states near the band gap has an effect on photoluminescence [30]. Therefore, it is reasonable to infer that photoluminescence is mainly related to halogen and lead atoms, namely octahedral atoms, and is independent of Cs atoms.

Moreover, as the halogen atom radius increases, the lattice becomes larger and the band gap becomes smaller, which is characteristic of halogen perovskites. However, according to the calculation results, only those belonging to the same type of equatorial plane can satisfy this changing law. In order to further explore the change rule of the band gap, we compared the lattice parameters of these materials and found that when the value of  $a^*b$  ( $a, b$  is the planar lattice parameter) is small, the band gap is larger (Table S1 within the Supplemental Material [41]). To show this change more clearly, the change in the band gap and  $S$  ( $S = a^*b$ ) with the ratio of I to Cl is plotted in Fig. 3. It can be seen intuitively from Fig. 3 that the decreasing trend of the band gap is almost consistent with the rising trend of  $S$ . The reason may be that the smaller lattice may have increased the nucleus's ability to bind electrons, thus improving the insulation of perovskite [31]. Therefore, the

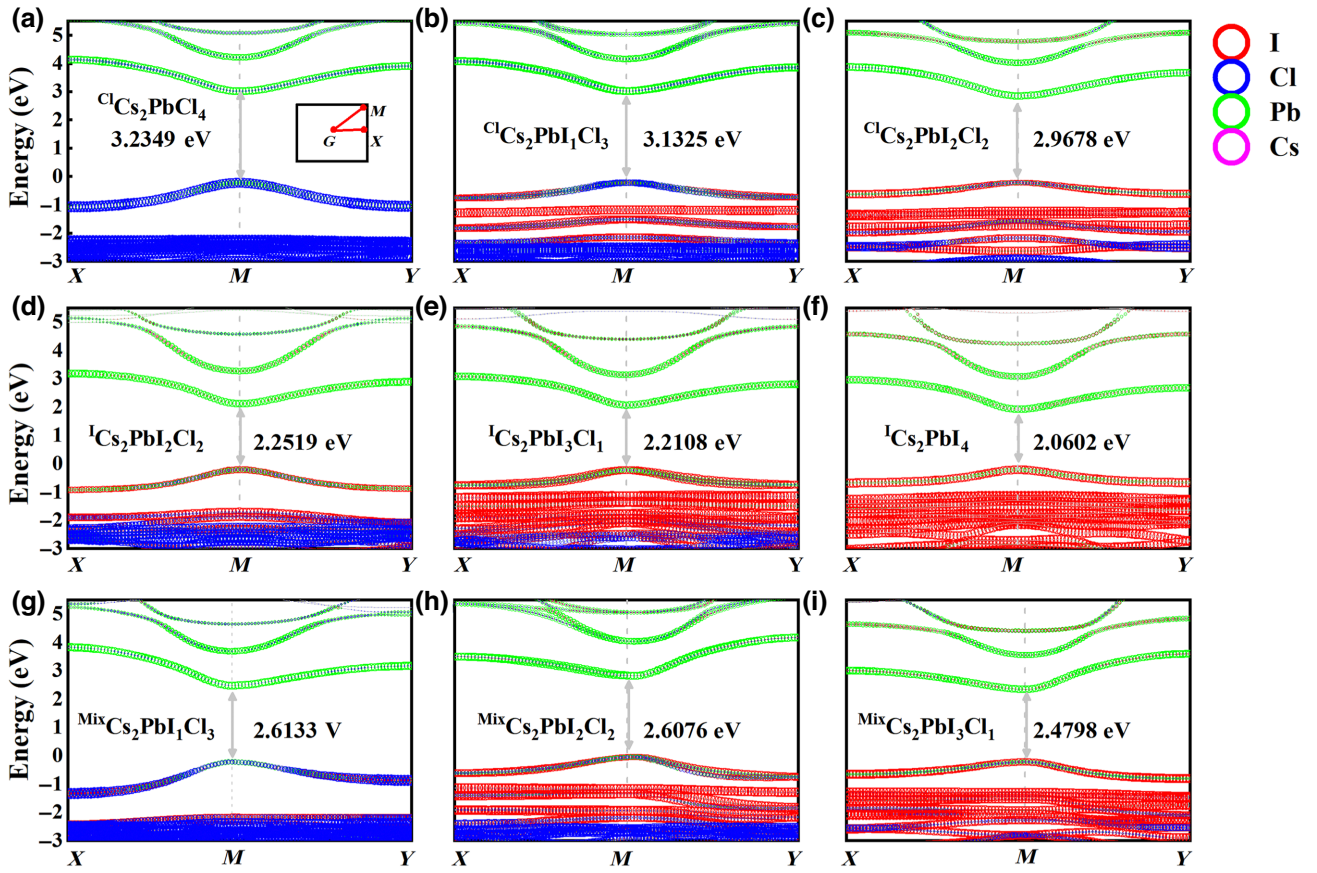


FIG. 2. Electronic band structure of 2D RP perovskite  $\text{Cs}_2\text{PbI}_x\text{Cl}_{4-x}$  calculated by the HSE + SOC method; (a)–(c) is the band structures of 2D RP perovskite  ${}^{\text{Cl}}\text{Cs}_2\text{PbCl}_4$ ,  ${}^{\text{Cl}}\text{Cs}_2\text{PbI}_1\text{Cl}_3$ , and  ${}^{\text{Cl}}\text{Cs}_2\text{PbI}_2\text{Cl}_2$ , respectively. (d)–(f) are the band structures of 2D RP perovskite  ${}^{\text{I}}\text{Cs}_2\text{PbI}_2\text{Cl}_2$ ,  ${}^{\text{I}}\text{Cs}_2\text{PbI}_3\text{Cl}_1$ , and  ${}^{\text{I}}\text{Cs}_2\text{PbI}_4$ , respectively. (g)–(i) are the band structures of 2D RP perovskite  ${}^{\text{Mix}}\text{Cs}_2\text{PbI}_1\text{Cl}_3$ ,  ${}^{\text{Mix}}\text{Cs}_2\text{PbI}_2\text{Cl}_2$ , and  ${}^{\text{Mix}}\text{Cs}_2\text{PbI}_3\text{Cl}_1$ , respectively.

regulation of the band gap by the halogen may be caused by the change in the lattice size by the halogen substitution.

The effective masses of 2D RP perovskite  $\text{Cs}_2\text{PbI}_x\text{Cl}_{4-x}$  ( $x = 0, 1, 2, 3, 4$ ) are calculated by the PBE and PBE + SOC method from Eq. (1) and the data are shown in Table S2 within the Supplemental Material [41] and Table I. No matter which method is used, for materials with the same equatorial plane structure, the average effective mass  $\langle m^* \rangle$  increases with the increase of I atom. Moreover, among the three types of equatorial planes, QEP-I has the smallest effective mass and QEP-Cl has the largest effective mass. Furthermore, we found that the hole effective mass, the electron effective mass  $\langle m_e \rangle$  and the average effective mass were significantly reduced after considering the SOC effect, indicating that the SOC effect has an obvious effect on the effective mass. The difference in effective quality calculated by the two methods is due to the presence of heavy-metal elements, making obvious differences in the band shape calculated by the PBE method and the PBE + SOC method. The band structures calculated by PBE method and PBE + SOC method are in Figs. S5 and S6 within the Supplemental Material [41], respectively.

Due to the greater dielectric confinement effect, the exciton effect of ultrathin monolayer 2D RP perovskite is very significant compared with multilayer 2D RP perovskite and three-dimensional perovskite [32]. Therefore, in order to describe the exciton effect of monolayer 2D RP perovskite  $\text{Cs}_2\text{PbI}_x\text{Cl}_{4-x}$ , the  $GW$  approximation combined with the BSE and the spin-orbit-coupling (SOC) effect is used to calculate the absorption spectrum as shown in Fig. 4. From Figs. 4(a)–4(i), it can be found that there is an obvious exciton absorption peak within the band gap for all nine materials. The existence of an exciton absorption peak broadens the light absorption range of materials, but due to the strong Coulomb potential between excitons, almost no more “free” electron-hole pairs are generated, so it does not contribute to the photovoltaic performance [2]. In contrast, the larger exciton binding energy leads to a wider absorption edge and increases the electron-hole recombination rate, thus promoting luminescence. Figures 4(a)–4(c), 4(d)–4(f), and 4(g)–4(i) represent the light absorption diagrams of three kinds of materials with QEP-I, QEP-Cl, and QEP-Mix structures, respectively. It can be seen from the calculated results that for materials with the

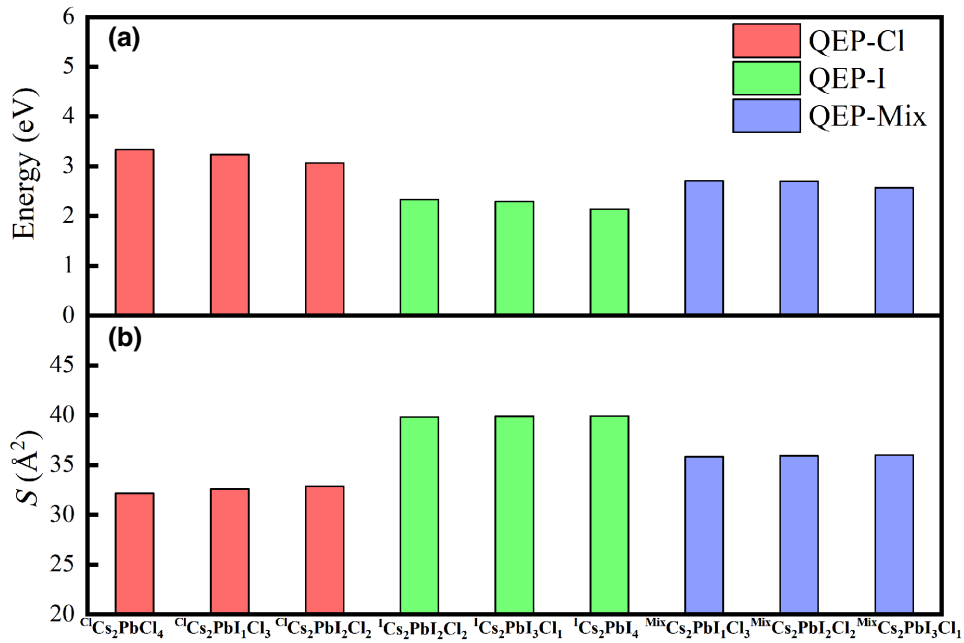


FIG. 3 (a) Shows the trend of the band-gap reduction for 2D RP perovskite  $\text{Cs}_2\text{PbI}_x\text{Cl}_{4-x}$ . (b) Show the variation trend of the area  $S$  of 2D RP perovskite  $\text{Cs}_2\text{PbI}_x\text{Cl}_{4-x}$ ; the area  $S$  is defined as the lattice parameter “ $a$ ” times the lattice parameter “ $b$ .” Different colors indicate the type of equatorial plane.

same equatorial plane structure, the smaller the ratio of I, the greater the intensity of the exciton absorption peak. In addition, by comparing the three kinds of  $\text{Cs}_2\text{PbI}_2\text{Cl}_2$  with different equatorial plane structures, it can be found that the exciton absorption peaks of  $\text{Cs}_2\text{PbI}_2\text{Cl}_2$  with a mixed equatorial plane are stronger.

The ground-state exciton-binding energy ( $E_b$ ) of  $\text{Cs}_2\text{PbI}_x\text{Cl}_{4-x}$  ( $x = 0, 1, 2, 3, 4$ ) and Bulk- $\text{Cs}_2\text{PbI}_2\text{Cl}_2$  was calculated on the basis of Eq. (2), as shown in Table II. The calculated dielectric constants are in Table S3 within the Supplemental Material [41]. Due to the more accurate calculation of the effective mass after considering the spin-orbit coupling, only the results of the  $E_b$  calculated by the PBE + SOC method are considered. As shown in

Table II, the exciton-binding energy of materials with the same halogen substitution type increases with the proportion of I atoms. Moreover, comparing the  $\text{Cs}_2\text{PbI}_2\text{Cl}_2$  of three different equatorial plane structures shows that the exciton-binding energy of QEP-Cl structures is greater than QEP-Mix and greater than QEP-I. The excitons discussed above represent free excitons calculated with the crystal structure fixed in the ground-state structure. Therefore, in order to determine the emission mechanism of the materials, we calculated the self-trapping energy of the nine materials by the  $\Delta\text{SCF}$  method and found that the self-trapping energy of all materials is zero, indicating that they do not exhibit self-trapping emission [33,34]. The emission of nine materials still belongs to free exciton

TABLE I. The effective masses  $m^*$  for 2D RP perovskite  $\text{Cs}_2\text{PbI}_x\text{Cl}_{4-x}$  ( $x = 0, 1, 2, 3, 4$ ) calculated by PBE + SOC method.

|   | Conduction band |          |                         | Valence band |          |                         | $m^*$ |
|---|-----------------|----------|-------------------------|--------------|----------|-------------------------|-------|
|   | $m_{xx}$        | $m_{yy}$ | $\langle m_e^* \rangle$ | $m_{xx}$     | $m_{yy}$ | $\langle m_h^* \rangle$ |       |
| $^{\text{Cl}}\text{Cs}_2\text{PbCl}_4$            | 0.254           | 0.254    | 0.254                   | 0.317        | 0.317    | 0.317                   | 0.286 |
| $^{\text{Cl}}\text{Cs}_2\text{PbI}_1\text{Cl}_3$  | 0.256           | 0.256    | 0.256                   | 0.454        | 0.454    | 0.454                   | 0.355 |
| $^{\text{Cl}}\text{Cs}_2\text{PbI}_2\text{Cl}_2$  | 0.268           | 0.268    | 0.268                   | 0.644        | 0.644    | 0.644                   | 0.456 |
| $^{\text{I}}\text{Cs}_2\text{PbI}_2\text{Cl}_2$   | 0.180           | 0.180    | 0.176                   | 0.259        | 0.259    | 0.259                   | 0.220 |
| $^{\text{I}}\text{Cs}_2\text{PbI}_3\text{Cl}_1$   | 0.178           | 0.178    | 0.178                   | 0.307        | 0.307    | 0.307                   | 0.243 |
| $^{\text{I}}\text{Cs}_2\text{PbI}_4$              | 0.179           | 0.179    | 0.179                   | 0.408        | 0.408    | 0.408                   | 0.294 |
| $^{\text{Mix}}\text{Cs}_2\text{PbI}_1\text{Cl}_3$ | 0.323           | 0.137    | 0.230                   | 0.361        | 0.179    | 0.270                   | 0.250 |
| $^{\text{Mix}}\text{Cs}_2\text{PbI}_2\text{Cl}_2$ | 0.142           | 0.321    | 0.232                   | 0.249        | 0.454    | 0.352                   | 0.292 |
| $^{\text{Mix}}\text{Cs}_2\text{PbI}_3\text{Cl}_1$ | 0.143           | 0.337    | 0.240                   | 0.306        | 0.550    | 0.428                   | 0.334 |
| Bulk- $\text{Cs}_2\text{PbI}_2\text{Cl}_2$        | 0.274           | 0.274    | 0.274                   | 0.600        | 0.600    | 0.600                   | 0.437 |

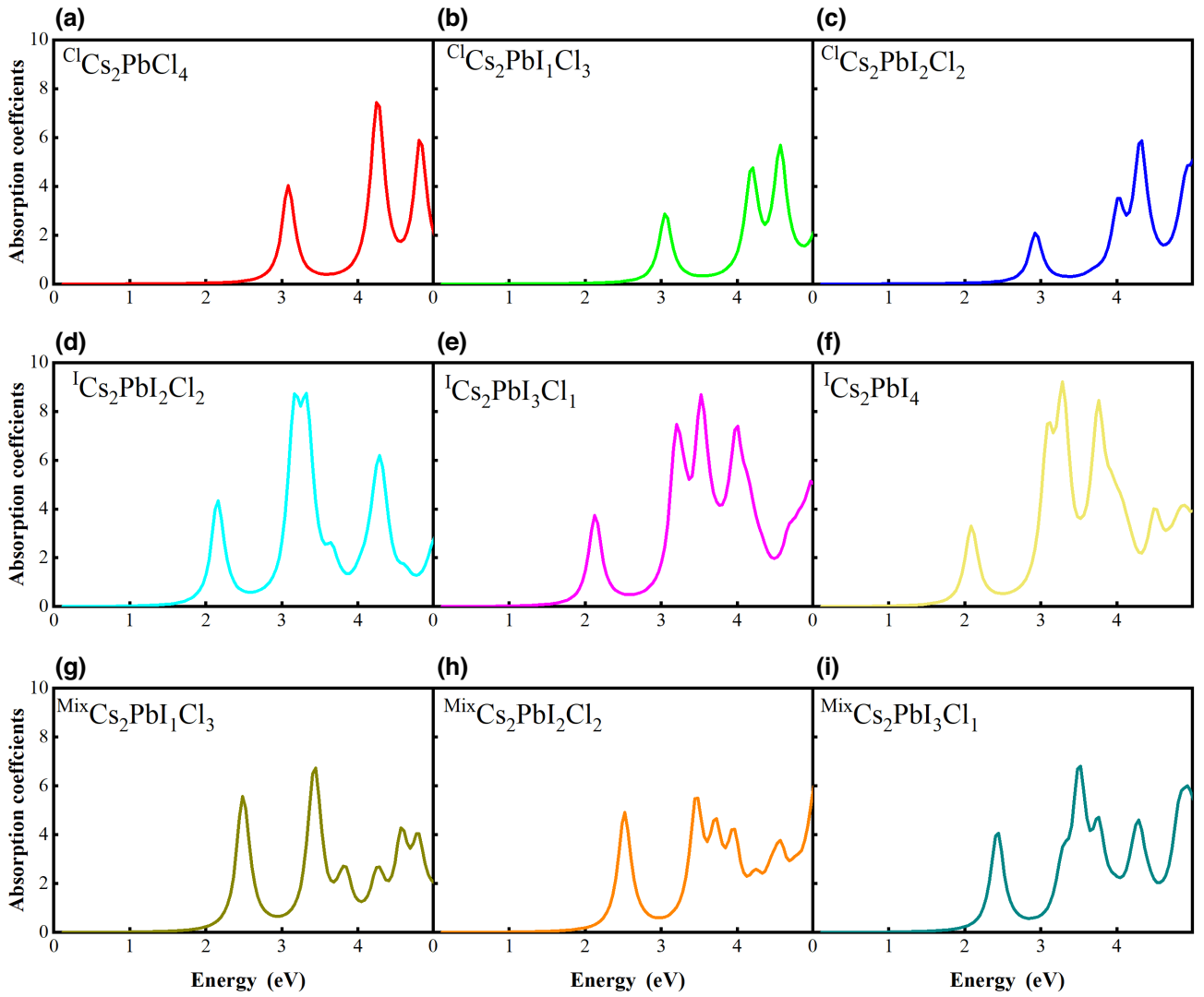


FIG. 4. Calculated light-absorption coefficients of monolayer 2D RP perovskite  ${}^{\text{Cl}}\text{Cs}_2\text{PbCl}_4$ ,  ${}^{\text{Cl}}\text{Cs}_2\text{PbI}_1\text{Cl}_3$ ,  ${}^{\text{Cl}}\text{Cs}_2\text{PbI}_2\text{Cl}_2$ ,  ${}^{\text{I}}\text{Cs}_2\text{PbI}_2\text{Cl}_1$ ,  ${}^{\text{I}}\text{Cs}_2\text{PbI}_3\text{Cl}_1$ ,  ${}^{\text{I}}\text{Cs}_2\text{PbI}_4$ ,  ${}^{\text{Mix}}\text{Cs}_2\text{PbI}_1\text{Cl}_3$ ,  ${}^{\text{Mix}}\text{Cs}_2\text{PbI}_2\text{Cl}_2$ , and  ${}^{\text{Mix}}\text{Cs}_2\text{PbI}_3\text{Cl}_1$ .

recombination. Therefore, the photoluminescence emission energy ( $E_{\text{PL}}$ ) of the material can be obtained using the formula  $E_{\text{PL}} = E_{\text{gap}} - E_b$  [35]. The calculated photoluminescence emission energy is shown in Table II. It can be found from the table for materials with the same replacement type, the photoluminescence emission energy decreases as the proportion of I atoms increases. In addition, to verify the reliability of our method, the photoluminescence emission energy of Bulk- $\text{Cs}_2\text{PbI}_2\text{Cl}_2$  is also calculated, and the calculated value (3.03 eV) is in excellent agreement with the experimental value (3.01 eV) [29].

The photoluminescence quantum yield (PLQY) is a key parameter characterizing the properties of luminescent materials, which is defined as the ratio of the radiative recombination rate to the sum of the nonradiative recombination rate and radiative recombination rate. Therefore,

increasing the radiation recombination rate is a strategy to increase PLQY. According to Fermi's golden rule, the radiative recombination rate is proportional to the transition dipole moment. In Ref. [20], the changing trend of PLQY of  $\text{Cs}_2\text{Ag}_{1-x}\text{Na}_x\text{InCl}_6$  related to sodium content was explored by plotting the transition dipole moment as a function of the sodium replacement ratio, which was in good agreement with the experiment [36]. The trend of transition dipole moment is consistent with the trend of PLQY and has been confirmed in other reports [37,38]. Therefore, this paper adopted the same method to study the changes of PLQY of  $\text{Cs}_2\text{PbI}_x\text{Cl}_{4-x}$  related to the halogen composition and position, as shown in Fig. 5. The squares of the transition dipole moments of the nine materials were calculated using vaspkit 1.2.5 code [39]. Figure 5 shows that for 2D RP perovskite materials with the same equatorial plane, the squares of the transition dipole

TABLE II. Exciton-binding energy and photoluminescence emission energy of monolayer of 2D RP perovskite  $\text{Cs}_2\text{PbI}_x\text{Cl}_{4-x}$  ( $x = 0, 1, 2, 3, 4$ ) and Bulk- $\text{Cs}_2\text{PbI}_2\text{Cl}_2$ .

|         | Exciton-binding energies (meV)                    | $E_{\text{PL}}$ (eV) |
|---------|---|----------------------|
| QEP-Cl  | $^{\text{Cl}}\text{Cs}_2\text{PbCl}_4$            | 316.87               |
|         | $^{\text{Cl}}\text{Cs}_2\text{PbI}_1\text{Cl}_3$  | 342.91               |
|         | $^{\text{Cl}}\text{Cs}_2\text{PbI}_2\text{Cl}_2$  | 374.00               |
| QEP-I   | $^{\text{I}}\text{Cs}_2\text{PbI}_2\text{Cl}_2$   | 150.71               |
|         | $^{\text{I}}\text{Cs}_2\text{PbI}_3\text{Cl}_1$   | 151.96               |
|         | $^{\text{I}}\text{Cs}_2\text{PbI}_4$              | 160.11               |
| QEP-Mix | $^{\text{Mix}}\text{Cs}_2\text{PbI}_1\text{Cl}_3$ | 217.55               |
|         | $^{\text{Mix}}\text{Cs}_2\text{PbI}_2\text{Cl}_2$ | 232.21               |
|         | $^{\text{Mix}}\text{Cs}_2\text{PbI}_3\text{Cl}_1$ | 234.35               |
| Bulk    | $\text{Cs}_2\text{PbI}_2\text{Cl}_2$              | 31.67                |

moment gradually weakens as the composition of heavy halogen I atoms increases. In order to compare the differences between the three equatorial plane structures,  $^{\text{Cl}}\text{Cs}_2\text{PbI}_2\text{Cl}_2$ ,  $^{\text{I}}\text{Cs}_2\text{PbI}_2\text{Cl}_2$ , and  $^{\text{Mix}}\text{Cs}_2\text{PbI}_2\text{Cl}_2$  were analyzed, and the results show that the squares of the transition dipole moment of  $^{\text{Mix}}\text{Cs}_2\text{PbI}_2\text{Cl}_2$  are the largest among the three. Therefore, among the nine materials, we predict that  $^{\text{Mix}}\text{Cs}_2\text{PbI}_1\text{Cl}_3$  may have the largest PLQY. The transition dipole moment is positively correlated with the overlap degree of the electron wave function and the hole wave function. Therefore, we speculate that the change in

halogen distribution may lead to the change of the overlap degree in the hole wave function and the electron wave function, which leads to the change of the transition dipole moment. To confirm our conjecture, we plot partial charge density diagrams of  $^{\text{Mix}}\text{Cs}_2\text{PbI}_1\text{Cl}_3$  and  $^{\text{Cl}}\text{Cs}_2\text{PbI}_2\text{Cl}_2$  (see Fig. S8 within the Supplemental Material [41]). It can be clearly seen from the figure that the overlap degree of electron and hole wave functions in  $^{\text{Mix}}\text{Cs}_2\text{PbI}_1\text{Cl}_3$  is significantly greater than that of  $^{\text{Cl}}\text{Cs}_2\text{PbI}_2\text{Cl}_2$ , which confirms our guess. Moreover, in order to evaluate the stability of  $\text{Cs}_2\text{PbI}_x\text{Cl}_{4-x}$  ( $x = 0, 1, 2, 3, 4$ ), the thermal stability of the structure was measured on the basis of AIMD simulation. Figures S9(a)–S9(i) within the Supplemental Material [41] is the result of the simulation calculation, which shows that the total energy as a function fluctuates with the test time. It is not difficult to find that with the change of time, the energy fluctuates only in a small range. Moreover, the chemical bond is not broken and the lattice parameters remain unchanged during the whole simulation process, which indicates that the structure should be stable at room temperature [28,40].

#### IV. CONCLUSION

In summary, we calculate the band structure, light absorption, photoluminescence emission energy, the transition dipole moments of monolayer 2D RP perovskite

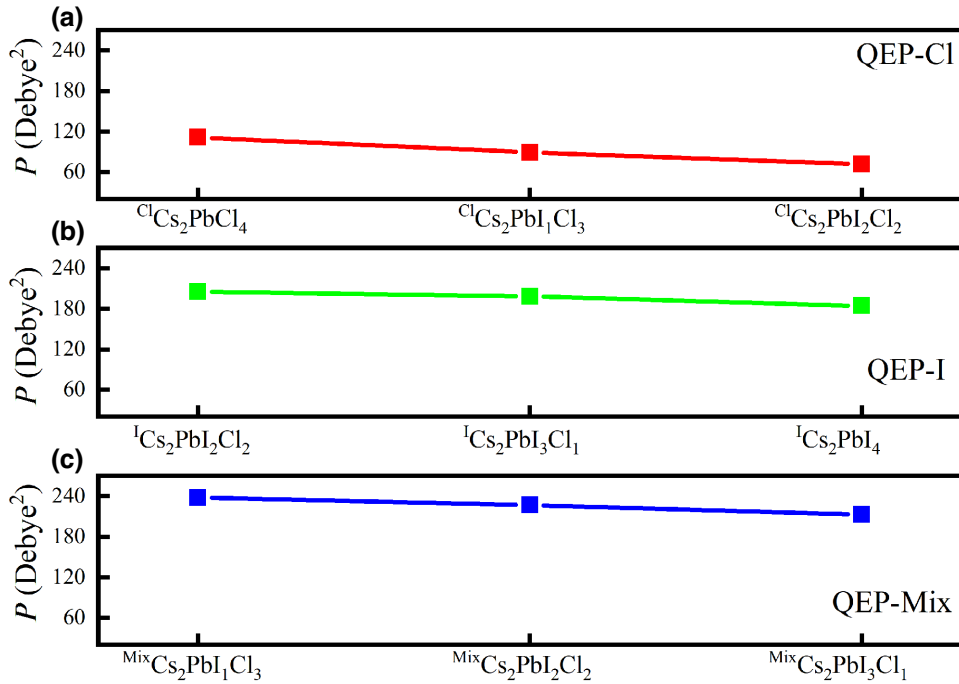


FIG. 5. The squares of the transition dipole moment of 2D all-inorganic perovskite  $\text{Cs}_2\text{PbI}_x\text{Cl}_{4-x}$  from the highest valence band to the lowest conduction band. (a) Represents the squares of the transition dipole moment of  $^{\text{Cl}}\text{Cs}_2\text{PbCl}_4$ ,  $^{\text{Cl}}\text{Cs}_2\text{PbI}_1\text{Cl}_3$ , and  $^{\text{Cl}}\text{Cs}_2\text{PbI}_2\text{Cl}_2$  with QEP-Cl structure; (b) represents the squares of the transition dipole moment of  $^{\text{I}}\text{Cs}_2\text{PbI}_2\text{Cl}_2$ ,  $^{\text{I}}\text{Cs}_2\text{PbI}_3\text{Cl}_1$ , and  $^{\text{I}}\text{Cs}_2\text{PbI}_4$  with QEP-I structure; (c) represents the squares of the transition dipole moment spectra of  $^{\text{Mix}}\text{Cs}_2\text{PbI}_1\text{Cl}_3$ ,  $^{\text{Mix}}\text{Cs}_2\text{PbI}_2\text{Cl}_2$ , and  $^{\text{Mix}}\text{Cs}_2\text{PbI}_3\text{Cl}_1$  with QEP-Mix structure.

$\text{Cs}_2\text{PbI}_x\text{Cl}_{4-x}$ , and discuss the regulation of halogen composition and halogen position on these properties. According to the calculation results, the regulatory law of halogen on 2D RP mixed halogen perovskite was obtained. The regulation of the band structure by halogen shows that the band structure and the band gap of materials with the same halogen substitution type are relatively close, and the size of the band gap is fine tuned by the halogen composition. The regulation of the exciton effect by halogen is that the absorption peak decreases and the exciton-binding energy increases for materials with the same halogen substitution type with the increase of I atom. The regulation of photoluminescence emission energy by halogen is that for structures with the same halogen substitution type, the photoluminescence emission energy decreases with the increase of the proportion of I atoms. The PLQY of nine materials was qualitatively compared by calculating the squares of the transition dipole moments of the materials. The results show that the Cl-rich materials with the mixed equatorial plane structures are more favorable for luminescence. Our study explains the reasons why some mixed halogen perovskites have better luminescence properties than single halogen perovskites and shows the regulation rules, which will provide theoretical guidance for the experimental design of more excellent luminescent materials.

### ACKNOWLEDGMENTS

The authors thank the Changsha Supercomputer Center for computation. This work is supported by the National Natural Science Foundation of China (Grants No. 51972103 and No. 21938002)

- [1] S. Adjokatsé, H.-H. Fang, and M. A. Loi, Broadly tunable metal halide perovskites for solid-state light-emission applications, *Mater. Today* **20**, 413 (2017).
- [2] Y. Q. Zhao, Q. R. Ma, B. Liu, Z. L. Yu, J. Yang, and M. Q. Cai, Layer-dependent transport and optoelectronic property in two-dimensional perovskite:  $(\text{PEA})_2\text{PbI}_4$ , *Nanoscale* **10**, 8677 (2018).
- [3] L.-Y. Pan, Y.-F. Ding, Z.-L. Yu, Q. Wan, B. Liu, and M.-Q. Cai, Layer-dependent optoelectronic property for all-inorganic two-dimensional mixed halide perovskite  $\text{Cs}_2\text{PbI}_2\text{Cl}_2$  with a Ruddlesden-Popper structure, *J. Power Sources* **451**, 227732 (2020).
- [4] M.-W. Zeng, Y.-Q. Zhao, and M.-Q. Cai, Effects of Halogen Substitution on the Optoelectronic Properties of Two-Dimensional All-Inorganic Double Perovskite  $\text{Cs}_4\text{AgBiX}_8$  ( $X = \text{Cl}, \text{Br}, \text{I}$ ) with Ruddlesden-Popper Structure, *Phys. Rev. Appl.* **16**, 054019 (2021).
- [5] C. Chen, Y. Kuai, X. Li, J. Hao, L. Li, Y. Liu, X. Ma, L. Wu, and P. Lu, Impact of halogen substitution on the electronic and optical properties of 2D lead-free hybrid perovskites, *J. Phys. Chem. C* **125**, 15742 (2021).
- [6] C. Pareja-Rivera, J. A. Morán-Muñoz, A. P. Gómora-Figueroa, V. Jancik, B. Vargas, J. Rodríguez-Hernández, and D. Solis-Ibarra, Optimizing broadband emission in 2D halide perovskites, *Chem. Mater.* **34**, 9344 (2022).
- [7] M. Zhang, H. Yu, M. Lyu, Q. Wang, J. H. Yun, and L. Wang, Composition-dependent photoluminescence intensity and prolonged recombination lifetime of perovskite  $\text{CH}_3\text{NH}_3\text{PbBr}_{(3-x)}\text{Cl}_{(x)}$  films, *Chem. Commun.* **50**, 11727 (2014).
- [8] X.-Z. Deng, Q.-Q. Zhao, Y.-Q. Zhao, and M.-Q. Cai, Theoretical study on photoelectric properties of lead-free mixed inorganic perovskite  $\text{RbGe}_{1-x}\text{Sn}_x\text{I}_3$ , *Curr. Appl. Phys.* **19**, 279 (2019).
- [9] Z. Xu, M. Chen, and S. F. Liu, Layer-dependent ultrahigh-mobility transport properties in all-inorganic two-dimensional  $\text{Cs}_2\text{PbI}_2\text{Cl}_2$  and  $\text{Cs}_2\text{SnI}_2\text{Cl}_2$  perovskites, *J. Phys. Chem. C* **123**, 27978 (2019).
- [10] X. Z. Deng, J. R. Zhang, Y. Q. Zhao, Z. L. Yu, J. L. Yang, and M. Q. Cai, The energy band engineering for the high-performance infrared photodetectors constructed by CdTe/MoS<sub>2</sub> heterojunction, *J. Phys.: Condens. Matter.* **32**, 065004 (2020).
- [11] D. B. Straus and C. R. Kagan, Electrons, excitons, and phonons in two-dimensional hybrid perovskites: Connecting structural, optical, and electronic properties, *J. Phys. Chem. Lett.* **9**, 1434 (2018).
- [12] Q. Chen, L.-M. Tang, K.-Q. Chen, and H.-K. Zhao, Heat generated by electrical current in a mesoscopic system perturbed by alternating current fields, *J. Appl. Phys.* **114**, 084301 (2013).
- [13] L.-J. Wu, Y.-Q. Zhao, C.-W. Chen, L.-Z. Wang, B. Liu, and M.-Q. Cai, First-principles hybrid functional study of the electronic structure and charge carrier mobility in perovskite  $\text{CH}_3\text{NH}_3\text{SnI}_3$ , *Chin. Phys. B* **25**, 107202 (2016).
- [14] H. Ying, W.-X. Zhou, K.-Q. Chen, and G. Zhou, Negative differential resistance induced by the Jahn–Teller effect in single molecular Coulomb blockade devices, *Comput. Mater. Sci.* **82**, 33 (2014).
- [15] A. Splendiani, L. Sun, Y. Zhang, T. Li, J. Kim, C.-Y. Chim, G. Galli, and F. Wang, Emerging photoluminescence in monolayer MoS<sub>2</sub>, *Nano Lett.* **10**, 1271 (2010).
- [16] K. F. Mak, C. Lee, J. Hone, J. Shan, and T. F. Heinz, Atomically Thin MoS<sub>2</sub>: A New Direct-Gap Semiconductor, *Phys. Rev. Lett.* **105**, 136805 (2010).
- [17] Diana Y. Qiu, Felipe H. da Jornada, and Steven G. Louie, Optical Spectrum of MoS<sub>2</sub>: Many-Body Effects and Diversity of Exciton States, *Phys. Rev. Lett.* **111**, 216805 (2013).
- [18] H. Mathieu, P. Lefebvre, and P. Christol, Simple analytical method for calculating exciton binding energies in semiconductor quantum wells, *Phys. Rev. B* **46**, 4092 (1992).
- [19] M. Wang, A. Krasnok, T. Zhang, L. Scarabelli, H. Liu, Z. Wu, L. M. Liz-Marzán, M. Terrones, A. Alù, and Y. Zheng, Tunable Fano resonance and plasmon-exciton coupling in single Au nanotriangles on monolayer WS<sub>2</sub> at room temperature, *Adv. Mater.* **30**, 1705779 (2018).
- [20] C. Otero-Martinez, J. Ye, J. Sung, I. Pastoriza-Santos, J. Perez-Juste, Z. Xia, A. Rao, R. L. Z. Hoye, and L. Polavarapu, Colloidal metal-halide perovskite nanoplatelets: Thickness-controlled synthesis, properties, and application in light-emitting diodes, *Adv. Mater.* **34**, 2107105 (2022).



- [21] D. Thrithamarassery Gangadharan and D. Ma, Searching for stability at lower dimensions: current trends and future prospects of layered perovskite solar cells, *Energy Environ. Sci.* **12**, 2860 (2019).
- [22] J. Quan, S. Yu, B. Xing, X. He, and L. Zhang, Two-dimensional Ruddlesden-Popper halide perovskite solar absorbers with short-chain interlayer spacers, *Phys. Rev. Mater.* **6**, 065405 (2022).
- [23] G. Y. Jia, Y. Liu, J. Y. Gong, D. Y. Lei, D. L. Wang, and Z. X. Huang, Excitonic quantum confinement modified optical conductivity of monolayer and few-layered  $\text{MoS}_2$ , *J. Mater. Chem. C* **4**, 8822 (2016).
- [24] Z. Xu, X. Jiang, H. P. Cai, K. Chen, X. Yao, and Y. Feng, Toward a general understanding of exciton self-trapping in metal halide perovskites, *J. Phys. Chem. Lett.* **12**, 10472 (2021).
- [25] X. Jiang, Z. Xu, Y. Zheng, J. Zeng, K. Q. Chen, and Y. Feng, A first-principles study of exciton self-trapping and electric polarization in one-dimensional organic lead halide perovskites, *Phys. Chem. Chem. Phys.* **24**, 17323 (2022).
- [26] A. Hellman, B. Razaznejad, and B. I. Lundqvist, Potential-energy surfaces for excited states in extended systems, *J. Chem. Phys.* **120**, 4593 (2004).
- [27] D. L. Busipalli, K.-Y. Lin, S. Nachimuthu, and J.-C. Jiang, Enhanced moisture stability of cesium lead iodide perovskite solar cells—a first-principles molecular dynamics study, *Phys. Chem. Chem. Phys.* **22**, 5693 (2020).
- [28] X. Huang, Y. Wang, Y. Weng, Z. Yang, and S. Dong, Stability, electronic, and optical properties of lead-free halide double perovskites  $(\text{CH}_3\text{NH}_3)_2\text{InBiX}_6$  ( $X = \text{halogen}$ ), *Phys. Rev. Mater.* **4**, 104601 (2020).
- [29] J. Li, Q. Yu, Y. He, C. C. Stoumpos, G. Niu, G. G. Trimarchi, H. Guo, G. Dong, D. Wang, L. Wang, and M. G. Kanatzidis,  $\text{Cs}_2\text{PbI}_2\text{Cl}_2$ , All-inorganic two-dimensional Ruddlesden-Popper mixed halide perovskite with optoelectronic response, *J. Am. Chem. Soc.* **140**, 11085 (2018).
- [30] A. Molina-Sánchez, Excitonic states in semiconducting two-dimensional perovskites, *ACS Appl. Energy Mater.* **1**, 6361 (2018).
- [31] B. Zhang, H. Zhang, J. Lin, and X. Cheng, A time-dependent density functional study on optical response in all-inorganic lead-halide perovskite nanostructures, *Int. J. Quantum Chem.* **120**, e26232 (2020).
- [32] K. Tanaka and T. Kondo, Bandgap and exciton binding energies in lead-iodide-based natural quantum-well crystals, *Sci. Technol. Adv. Mater.* **4**, 599 (2003).
- [33] X. Li, P. Guo, M. Kepenekian, I. Hadar, C. Katan, J. Even, C. C. Stoumpos, R. D. Schaller, and M. G. Kanatzidis, Small cyclic diammonium cation templated (110)-oriented 2D halide ( $X = \text{I, Br, Cl}$ ) perovskites with white-light emission, *Chem. Mater.* **31**, 3582 (2019).
- [34] E. J. Crace, A. C. Su, and H. I. Karunadasa, Reliably obtaining white light from layered halide perovskites at room temperature, *Chem. Sci.* **13**, 9973 (2022).
- [35] L. Lian, M. Zheng, P. Zhang, Z. Zheng, K. Du, W. Lei, J. Gao, G. Niu, D. Zhang, T. Zhai, S. Jin, J. Tang, X. Zhang, and J. Zhang, Photophysics in  $\text{Cs}_3\text{Cu}_2\text{X}_5$  ( $X = \text{Cl, Br, I}$ ): Highly luminescent self-trapped excitons from local structure symmetrization, *Chem. Mater.* **32**, 3462 (2020).
- [36] J. Luo, X. Wang, S. Li, J. Liu, Y. Guo, G. Niu, L. Yao, Y. Fu, L. Gao, Q. Dong, *et al.*, Efficient and stable emission of warm-white light from lead-free halide double perovskites, *Nature* **563**, 541 (2018).
- [37] Y. Wang, Q. Song, W. Hu, D. Wang, L. Peng, T. Shi, X. Liu, Y. Zhu, and J. Lin, Temperature-driven phase transition and transition dipole moment of two-dimensional  $(\text{BA})_2\text{CsPb}_2\text{Br}_7$  perovskite, *Phys. Chem. Chem. Phys.* **23**, 16341 (2021).
- [38] C. Xue, H. Huang, S. Nishihara, V. Biju, X. M. Ren, and T. Nakamura, Inorganic chain mediated excitonic properties in one-dimensional lead halide hybrid perovskites, *J. Phys. Chem. Lett.* **13**, 7405 (2022).
- [39] U. Herath, P. Tavazde, X. He, E. Bousquet, S. Singh, F. Muñoz, and A. H. Romero, PyProcar: A Python library for electronic structure pre/post-processing, *Comput. Phys. Commun.* **251**, 107080 (2020).
- [40] X.-J. Wu, Y.-F. Ding, B. Liu, J.-L. Yang, and M.-Q. Cai, Halogen's effect on the photoelectric properties of two-dimensional organic-inorganic hybrid perovskite  $(\text{MTEA})_2\text{MAPb}_2\text{X}_7$  ( $X = \text{Cl, Br, I}$ ) with a Ruddlesden-Popper structure, *Appl. Phys. Lett.* **121**, 211103 (2022).
- [41] See the Supplemental Material at <http://link.aps.org/supplemental/10.1103/PhysRevApplied.20.024047> for additional details, including atomic structures, band structures, state densities, partial charge density, and thermal stability.